Dual-Mode High-*Q* Multiphysics Sensor Based on the Evanescent Wave in the InSb Photonic Crystals

Jia-Tao Zhang, Si-Si Rao, and Hai-Feng Zhang

***Abstract*—In this article, a dual-mode multiphysical quantity sensor is designed based on the indium antimonide (InSb) photonic crystals (PCs), which are using the evanescent wave principle. The sensor is mainly composed of InSb and three isotropic dielectrics, one layer of which is the dielectric to be measured. By adjusting the magnetic field strength, the operation modes of the structure can be controlled to switch between the transmittance and interference absorption cases.**

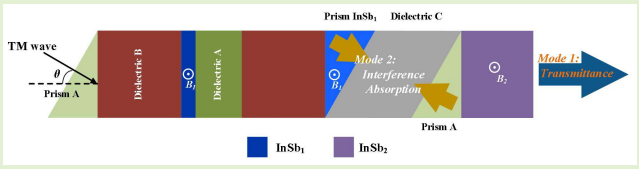

In a transmittance mode, the dielectric to be measured is set to the air layer, and sensing of magnetic field strength, thermodynamic temperature, and incident angle can be achieved. While for the interference absorption mode, the refractive index and the thickness of the dielectric to be measured can be obtained. It is worth mentioning that the linear range for sensing the dielectric thickness and refractive index in this mode is theoretically infinite based on the principle of interferometric light. In addition to the benefits of the introduction of the evanescent wave structure, the sensor has extremely high-quality factors (*Q*) for the measurement of various physical quantities. Thus, this design is likely to reveal great potential in the field of physical measurements.

***Index Terms*—Evanescent wave, indium antimonide (InSb), interference, multiphysics sensor, photonic crystals (PCs).**

I. Introduction

PEOPLE describe artificial periodic dielectric structures with photonic bandgaps (PBGs) as photonic crystals (PCs) [1], [2], [3], [4], [5], whose most remarkable feature is that they can impede the transmission of electromagnetic (EM) waves of specific frequencies. Based on this excellent optical property, PCs have been widely investigated for decades, and numerous works have also pointed out that the existence of PBGs is perfectly suited for the design of micro- and nanodevices, such as sensors [6], [7], [8], [9], semiconductor lasers [10], [11], optical switches [12], and so on. Particularly for sensors, PCs with small sizes, high-quality factors (Q), and flexible designs are becoming increasingly popular among researchers. Furthermore, in terms of sensitivity (S), the figure of merit (FOM), and other metrics for sensor quality, the PCs could also perform admirably. Currently, there is a lot of existing work with excellent results based on this structure. Edappadikkunnummal et al. [13] proposed a 1-D PC-based refractive index sensor for hemoglobin concentration measurement with a sensitivity of 144.5 nm/RIU in the working interval. Ge et al. [14] used the structure of magnetic fluid defects to design a sensor that could be used for both magnetic field and temperature dual scales with a sensitivity and an FOM of 0.817 nm/Oe and 17.439 Oe^{-1} in the magnetic field variation range of 30–90 Oe, and the theoretical sensitivity of temperature sensing can reach 72.4 pm/°C. Furthermore, the structure reported by Elshahat et al. [15] has excellent indications in terms of tunability and performance, reaching a sensitivity of 603.753 nm/RIU, FOM = 8147.814 RIU^{-1}, for sensing glucose solutions with concentrations between 0% and 30% by introducing a layer of defects in both PCs. The PCs embody excellent and irreplaceable performance in the design of the sensor structure.

Based on the general PCs structure, the Q value of the sensor can be significantly improved by introducing the evanescent wave [16], [17], [18] principle. It is well known that when an EM wave enters an optical sparse medium from an optical density media, total reflection occurs when its incident angle is greater than a certain threshold, and the evanescent wave exists at the interface of the two dielectrics. However, if the optical sparse medium is thin enough, EM waves of certain specific frequencies can pass through virtually losslessly, exhibiting one or several spikes in the

Manuscript received 17 October 2022; revised 5 December 2022; accepted 11 December 2022. Date of publication 20 December 2022; date of current version 31 January 2023. The associate editor coordinating the review of this article and approving it for publication was Prof. Hsin-Ying Lee. *(Corresponding author: Hai-Feng Zhang.)*

The authors are with the College of Electronic and Optical Engineering and the College of Flexible Electronics, Nanjing University of Posts and Telecommunications, Nanjing 210023, China (e-mail: hanlor@163.com; hanlor@njupt.edu.cn).

Digital Object Identifier 10.1109/JSEN.2022.3229320

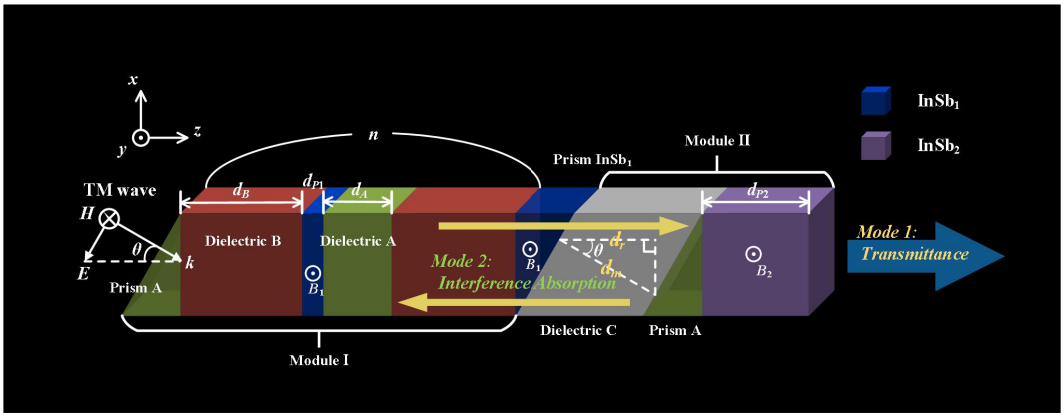

Fig. 1. Structure diagram of the designed sensor.

transmission spectrum, which is the reason for the ultrahigh-Q value of these sensors. In addition, the use of magnetron dielectrics in the structure generating the evanescent waves allows the manipulation of the transmission spectrum of the structure by external conditions. Among them, indium antimonide (InSb) [19], [20], [21] is a typical kind of these dielectrics, whose dielectrictensor changes with magnetic field strength, temperature, and other factors. This is also the key to the design of the dual-mode multiphysics sensor in this work.

There is another very intriguing phenomenon in physical optics, namely, the interference of light [22], [23]. When the phase difference between two beams of light is fixed and their vibration direction and frequency are the same, in other words, when the coherence condition is satisfied, interference occurs. In particular, if the amplitudes of the two beams are also equal and the phase difference is exactly π, the energy of the two will completely cancel when they meet, which is called destructive interference [23]. This is reflected by the absorptance in the PCs structure.

In this work, the structure is designed using a total of InSb and three other isotropic dielectrics, which is divided into two modules for generating evanescent waves and switching operation modes between transmittance and interference absorption, respectively. Sensing of magnetic field strength, thermodynamic temperature, and the incident angle is performed in transmittance mode, while interference absorption mode is used to measure the thickness and refractive index of dielectric C. Each result is calculated by the transfer matrix method (TMM) [24]. It is worth mentioning that the linear range of physical quantities measured in Mode 2 can theoretically extend to infinity. Table I lists the metrics of the sensors designed by other researchers compared with this work.

II. Theoretical Model

The structure of the designed sensor is shown in Fig. 1, where module I for generating evanescent waves is made up of dielectrics A, B, and InSb$_1$ and is designated by $(\mathrm{ABM_1})^n$ in this article, where n represents the number of periods of the structure. Module II consists of dielectric C, prism A, and InSb$_2$ to switch between the two modes. Magnetic fields of intensity B_1 and B_2 along the positive direction of the y-axis are introduced to the InSb layers in modules I and II, respectively. The thicknesses and refractive indices of the three isotropic dielectrics are denoted by d_A, d_B, d_m, n_A, n_B, and n_m. Dielectric C is used as the dielectric to be measured in the interference absorption mode, and the subscripts of its refractive index and thickness are m. The InSb layers in the two modules are denoted by subscripts $p1$ and $p2$, corresponding to refractive indices and thicknesses of n_{p1}, n_{p2}, d_{p1}, and d_{p2}, respectively. The thickness of one period in module I is $d = d_A + d_B + d_{p1}$. It should be noted that the propagation of EM waves in dielectric C is due to the coupling of the prisms on both sides, and the thickness of the layer should be the length of the hypotenuse of the right triangle d_m in Fig. 1; while the actual measurement requires the length of the cathetus d_r, when the EM wave is incident at an angle θ, there is a cosθ multiplicative relationship between d_m and d_r.

Under the action of the applied magnetic field, the dielectric tensor of InSb can be expressed as follows [19], [21]:

$$\hat{\varepsilon}_{\mathrm{InSb}} = \begin{bmatrix} \varepsilon_x & 0 & j\varepsilon_{xz} \\ 0 & \varepsilon_y & 0 \\ -j\varepsilon_{xz} & 0 & \varepsilon_z \end{bmatrix} \tag{1}$$

where

$$\varepsilon_x = \varepsilon_z = \varepsilon_\infty - \varepsilon_\infty \frac{\omega_p^2 (\omega + j\nu_c)}{\omega\left[(\omega + j\nu_c)^2 - \omega_c^2\right]} \tag{2a}$$

$$\varepsilon_y = \varepsilon_\infty - \varepsilon_\infty \frac{\omega_p^2}{\omega(\omega + j\nu_c)} \tag{2b}$$

$$\varepsilon_{xz} = \varepsilon_\infty \frac{\omega_p^2 \omega_c}{\omega\left[(\omega + j\nu_c)^2 - \omega_c^2\right]}. \tag{2c}$$

In the above equation, ε_∞ is the high-frequency limit permittivity and is fixed at 15.68 [20], ω is the angular frequency of the incident EM wave, and ω_p, ω_c, and ν_c represent the plasma frequency, cyclotron frequency, and the collision frequency of carriers, respectively. The cyclotron frequency is proportional to the magnetic field strength as $\omega_c = eB/m^*$, where e and m^* refer to the electron charge and the effective mass of the carrier; moreover, the relationship between m^* and the electron mass m_e is $m^* = 0.015m_e$ [20]. The plasma frequency ω_p is affected by the intrinsic carrier density, expressed as N in this article, and satisfies the equation $\omega_p = (\mathrm{Ne}^2/\varepsilon_0 m^*)^{1/2}$, where ε_0 is the permittivity

TABLE I
COMPARISON OF METRICS BETWEEN DIFFERENT SENSORS*

		Mode 1			Mode 2	
		Magnetic field strength	Thermodynamic temperature	Incident angle	Thickness	Refractive index
[13]	**L**	none	none	none	none	1.341~1.404 RIU
	S					144.50 nm/RIU
	Q					231.55
	FOM					43.787 RIU^{-1}
[14]	**L**	30~90 Oe	20~70 °C	none	none	none
	S	0.817 nm/Oe	/			
	Q	/	/			
	FOM	17.439 Oe^{-1}	72.4 $°C^{-1}$			
[15]	**L**	none	none	none	none	1.33230545~1.36797245 RIU
	S					603.753 nm/RIU
	Q					23340.27
	FOM					8147.814 RIU^{-1}
This work	**L**	1.2~2.0 T	230~250 K	28~32 degree	3.6~12.6 μm	1.12~1.42 RIU
	S	0.4848 THz/T	0.07037 THz/K	0.9983 THz/degree	0.001844 THz/μm	0.002438 THz/RIU
	Q	97457	102433	435060	140069	138715
	FOM	724.92 T^{-1}	110.14 K^{-1}	6522.15 $degree^{-1}$	133223 μm^{-1}	5.233 RIU^{-1}

*The thickness of one period is defined as 30 μm here; linear range, sensitivity, quality factor and figure of merit are denoted by L, S, Q and FOM, respectively. Both Q and FOM are the maximum values reached during the measurement.

in a vacuum. In this structure, the collision frequency of carriers of InSb in both modules (ν_{c1}, ν_{c2}) is set to $0.00001\omega_p$. It is also worth mentioning that N varies drastically with the thermodynamic temperature T_0, and has the following form [20]:

$$N(m^{-3}) = 5.76 \times 10^{20} T_0^{1.5} e^{\frac{-0.26}{2\times 8.625\times 10^{-5}\times T_0}}. \tag{3}$$

When the EM wave is incident in the form of TM polarization, based on the principle of TMM, the dielectric constant of InSb can be equated as follows [19], [20]:

$$\varepsilon_p = \frac{\varepsilon_x^2 - \varepsilon_{xz}^2}{\varepsilon_x} \tag{4}$$

and effective refractive index $n_p = \sqrt{\varepsilon_p}$.

Furthermore, the transfer matrix of the InSb layer is simplified as (5), shown at the bottom of the page, [19], [21], where $i = 1, 2$ indicates the InSb in the two modules, the subscripts x and z refer to the x- and z-directions, respectively, $k_{xi} = \omega/c \cdot n_{pi} \cdot \sin\theta_i, k_{zi} = \omega/c \cdot n_{pi} \cdot \cos\theta_i$, and $\eta_i = (\varepsilon_0/\mu_0)^{1/2} \cdot n_{pi}/\cos\theta_i$ for TM mode, where μ_0 is the magnetic permeability in a vacuum, and θ_i is the angle between the forward direction of the EM wave in InSb and the z-axis. As for general dielectrics, the transfer matrix has a simpler form

$$\mathbf{M_a} = \begin{bmatrix} \cos(k_{za}d_a) & -\frac{j}{\eta_a}\sin(k_{za}d_a) \\ -j\eta_a \sin(k_{za}d_a) & \cos(k_{za}d_a) \end{bmatrix}, \quad (a = A, B, m). \tag{6}$$

The transfer matrix of the whole structure can be obtained by multiplying the matrices of each layer, in turn, as follows:

$$\mathbf{M} = \mathbf{M_B} \cdot \left(\mathbf{M_{p1}} \cdot \mathbf{M_A} \cdot \mathbf{M_B}\right)^{n-1} \cdot \mathbf{M_m} \cdot \mathbf{M_{p2}}. \tag{7}$$

The prism in Fig. 1 is only applied to adjust the incident angle of EM waves and is not considered in the calculations of this work.

Using m_{pq} ($pq = 1, 2$) to refer to the four elements of the matrix $\mathbf{M}$, the transmission coefficient t and the reflection coefficient r of the whole structure can be calculated as follows [12], [14]:

$$t = \frac{2\eta_0}{(m_{11} + m_{12}\eta_{n+1})\eta_0 + (m_{21} + m_{22}\eta_{n+1})} \tag{8}$$

$$r = \frac{(m_{11} + m_{12}\eta_{n+1})\eta_0 - (m_{21} + m_{22}\eta_{n+1})}{(m_{11} + m_{12}\eta_{n+1})\eta_0 + (m_{21} + m_{22}\eta_{n+1})}. \tag{9}$$

Due to the coupling effect of the prism, η_0, η_{n+1} are numerically the same as η_A and η_{p1}, respectively. t and r take the

$$\mathbf{M_{pi}} = \begin{bmatrix} \cos(k_{zi}d_{pi}) + \frac{k_{xi}\varepsilon_{2i}}{k_{zi}\varepsilon_{1i}}\sin\left(k_{zi}d_{pi}\right) & -\frac{j}{\eta_i}\left[1 + \left(\frac{k_{xi}\varepsilon_{2i}}{k_{zi}\varepsilon_{1i}}\right)^2\right]\sin\left(k_{zi}d_{pi}\right) \\ -j\eta_i \sin\left(k_{zi}d_{pi}\right) & \cos(k_{zi}d_{pi}) - \frac{k_{xi}\varepsilon_{2i}}{k_{zi}\varepsilon_{1i}}\sin\left(k_{zi}d_{pi}\right) \end{bmatrix} \tag{5}$$

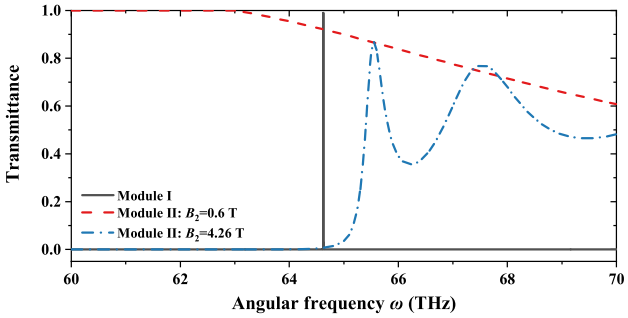

Fig. 2. Transmission spectrum of each module when acting individually.

square of the respective magnitude that is the transmittance and reflectance [19], [21]

$$T = |t|^2 \tag{10}$$

$$R = |r|^2 . \tag{11}$$

The absorptance then is called out as follows:

$$A = 1 - T - R. \tag{12}$$

III. Analysis and Discussion

In this article, for the structure of Fig. 1, the parameters of each layer of the dielectric are set as $d = 30\ \mu$m, $d_A = 0.32d$, $d_B = 0.58d$, $d_m = 0.6d$, $d_{p1} = 0.1d$, $d_{p2} = 0.5d$, $n_A = 3.8$, $n_B = 1.4$, and ambient temperature $T_0 = 240$; all EM waves are incident in TM mode. Dielectric C is normally set as an air layer; i.e., $n_m = 1$. $B_1 = 0.6$ T, the value of B_2 impacts the transmission of the whole structure and will be discussed in the following. It has been reported that the number of spikes in the transmission spectrum under the evanescent wave structure is equal to the number of periods of the structure n minus 1 [18]. Also, for sensors, only one spike is most convenient for practical applications. Based on the above principles, n in this work is selected as 2. In addition, the structures (A)BM_1 and $AB(M_1)$, which consist of a combination of prism and dielectric layers, are also considered as a period, where ( ) denotes the prism. The TM wave is incident at an angle of 30° perpendicular to the hypotenuse of the prism.

To better demonstrate the role of each module, the transmission spectra of the two modules when acting individually are provided in Fig. 2. It can be seen that when only module I exists, a transmission peak will appear at $\omega = 64.6238$ THz. Also, the function of module II is to facilitate mode switching. On the one hand, when the magnetic field $B_2 = 0.6$T is applied to the $InSb_2$ layer, the transmittance of module II at the frequency corresponding to the transmission peak is above 0.9, which can be approximated as transparent. In this case, the whole structure works in transmittance mode. On the other hand, when the intensity of B_2 becomes 4.26 T, module II exhibits a wide range of reflective properties. When the coherence condition is satisfied between the reflected EM and the incoming waves, interference will occur within the structure, and the original transmission peak is transformed into an absorption peak in this case, which corresponds to the interference absorption mode. The EM wave transmission properties in the two modes are shown in Fig. 3, The transmittance of the transmission peak in mode 1 can reach

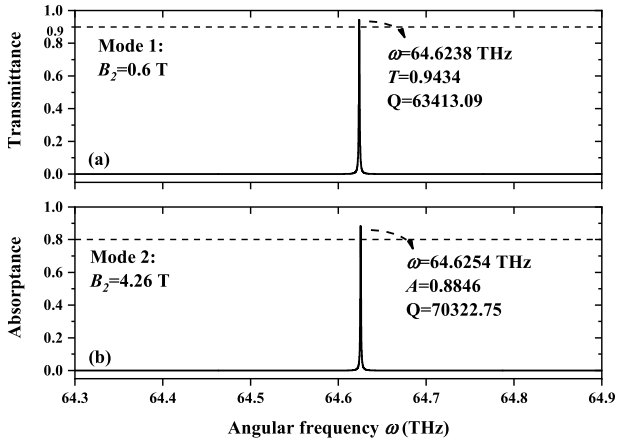

Fig. 3. Transmission properties of EM waves in structures under different applied magnetic fields. (a) Mode 1: transmittance, $B_2 = 0.6$ T. (b) Mode 2: interference absorption, $B_2 = 4.26$ T.

0.9434, and when switching to mode 2, the absorbance of the same frequency point can also reach 0.8846, indicating that the difference in sensing quantity between the two modes is clear, and the switching only requires adjusting the strength of the magnetic field, which is easy to achieve in practice.

Meanwhile, to demonstrate the successful generation of evanescent wave transmission, Fig. 4 simulates the distribution of the magnetic field in module I when the incident wave is incident at a frequency corresponding to the transmission peak and the general situation in contrast. Since the presence of module II is only used to change the transmission and interference absorption modes of the structure, it is not taken into account here. It can be found that after the transmission of the evanescent wave, the two layers of dielectric B with lower refractive index are equivalent to a resonant cavity at this time, and the energy of the incident EM wave is largely localized in the dielectric A and $InSb_1$ layers with higher refractive index in the real part and continuously oscillates and intensifies, which eventually manifests itself as a spike in the transmission spectrum. For the general case, the incident EM wave is totally reflected directly at the boundary between prism A and dielectric B and has not been localized. Notice the difference of about two orders of magnitude in the peak value of the norm of a magnetic field in the top graph compared to the bottom graph in Fig. 4, which shows the obvious resonance effect. It is also worth mentioning that there is a slight deviation in the transmission frequency point obtained from the simulation and the formula (approximately between 0.1 THz); after considering the impact of Module II, this is acceptable.

When the sensor is employed in transmittance mode, the evanescent wave structure of module I plays the primary role in the sensor's ability to measure the magnetic field strength, thermodynamic temperature, and incident angle, where the applied magnetic field and the ambient temperature have an impact on the InSb's cyclotron frequency ω_{c1} and plasma frequency ω_{p1}, respectively, and further influence the location of the transmission frequency point. In addition, according to the principle of evanescent wave formation, the difference in the incident angle of EM waves also leads to the offset

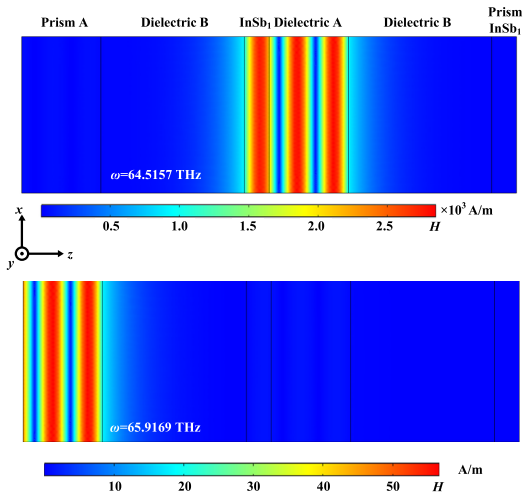

Fig. 4. Norm of magnetic field distribution in the structure when EM waves are incident at frequencies corresponding to the transmission peak ($\omega = 64.5157$ THz) and reflection band ($\omega = 65.9196$ THz).

of the transmission peak position. Based on these theories, the sensors in this work were designed. The results of the TMM calculations will be used to analyze the measurement indicators of each physical quantity in Section III. The sensor operates in mode 1, module II with an applied magnetic field $B_2 = 0.6$ T, module I as the magnetic field strength induction area, and the rest of the conditions are kept constant. The transmission spectra of the sensor at different magnetic field strengths B_1 are depicted in Fig. 5(a), where $B_1 = 1.2$–2.0 T is considered as the linear region of the measurement, and Fig. 5(b) provides the results after linear fitting. The relationship between the transmission frequency point and the applied magnetic field satisfies the equation $\omega = 0.4848B_1 + 64.19$. R-square, which is used for measuring linearity, is 0.9912. In general, this value can be considered acceptable for the linearity of the curve if it is greater than 0.99. The Q and FOM corresponding to some of the magnetic field strengths are given in Fig. 5(c) In the linear range, the values of Q are above 90 000, and the FOM stays around 700 T^{-1}, which are exceptionally high performance for the sensors.

The results concerning thermodynamic temperature sensing are all illustrated in Fig. 6(a) and (b). The linear range of this physical quantity is between 230 and 250 K (Celsius temperature −43.15 °C to −23.15 °C); at this point, the equation between the transmission peak frequency and the thermodynamic temperature is $\omega = 0.07037T_0 + 49.29$, and R-square is 0.9909, which meets the design requirements. The data in Fig. 6(c) reveal that the values of Q and FOM are still at an extremely high level, and Q can reach the values of 80 000–100 000 or more, and FOM is at least 87.74 K^{-1} and will increase to 110.14 K^{-1} when the temperature rises. A larger number of these indicators reflect a more accurate measurement of the sensor.

Finally, the sensing of the incident angle in mode 1 yields very remarkable data. The linear interval obtained from Fig. 7(a) is fit, as presented in Fig. 7(b). In the range of 28°–32°, the R-square of the fit curve is 0.9999, suggesting that the fit result has been essentially located on the straight line

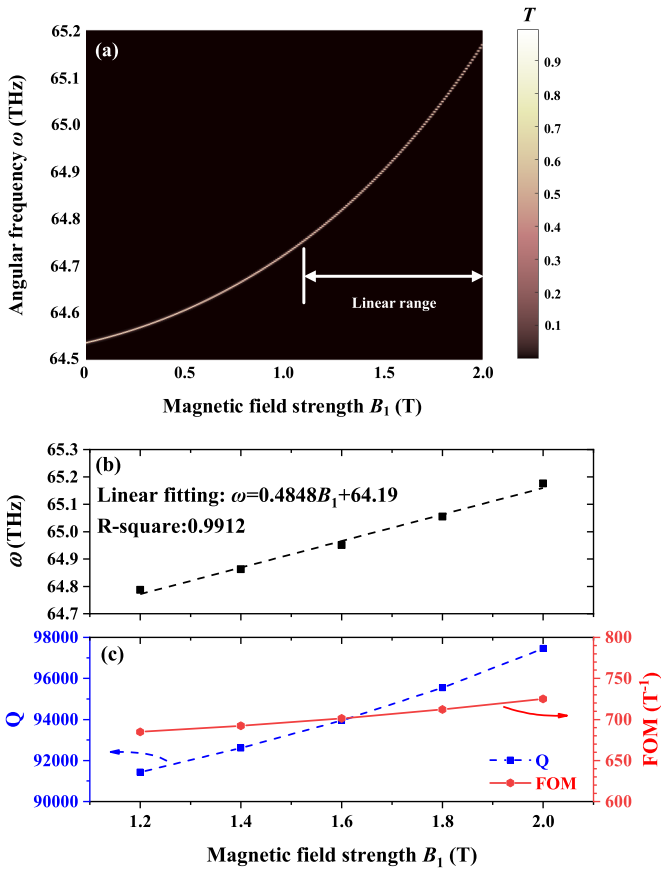

Fig. 5. (a) Transmission spectrum of the sensor at different magnetic field strengths B_1. (b) Transmission spectrum after fitting of linear range. (c) Corresponding Q and FOM at different B_1 values.

$\omega = 0.9983\theta + 34.66$. The results in Fig. 7(c) specify that the multiplication of Q and FOM due to the increase in angle is exponential. The maximum value of Q is 435 060, which is more than several times of another physical sensing indicator, and the value of FOM increases gradually from 242.95 to 6522.15 $degree^{-1}$ with the increase in measurement angle. The advantages of the high Q brought by the use of the evanescent wave principle are demonstrated here to the fullest extent.

Measurements of thickness and refractive index can be implemented in mode 2; in this case, the strength of magnetic field B_2 applied to the outside of module II is 4.26 T. The parameters of module I remain unchanged and are only used to generate a transmission spike, while the combined structure of prism A and $InSb_2$ layer can completely reflect the evanescent wave and keep its amplitude approximately constant. The superposition theory of light waves shows that two light waves with the same frequency and vibration direction meet at a certain point in space, and if the amplitude of both light waves is a, the combined amplitude A_s of the superposed light waves at that point is [23]

$$A_s = 4a^2 \cos^2 \frac{\delta}{2} \tag{13}$$

where δ is a phase difference between two light waves. Obviously, when $\delta = \pi$, the combined amplitude is zero, and the absorption of the structure tends to the maximum. If the optical path difference between two light waves is denoted

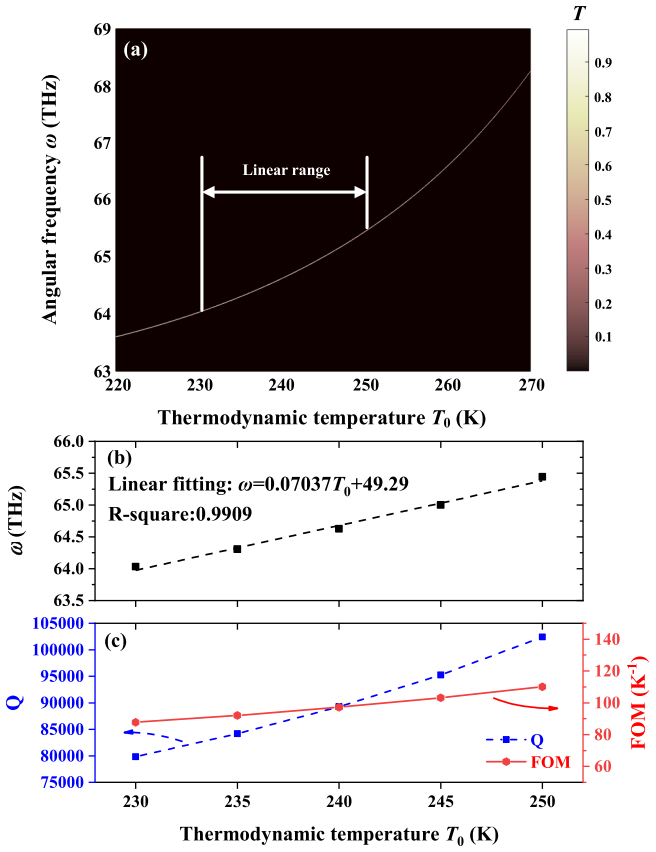

Fig. 6. (a) Transmission spectrum of the sensor at different thermodynamic temperatures T_0. (b) Transmission spectrum after fitting of linear range. (c) Corresponding Q and FOM at different T_0 values.

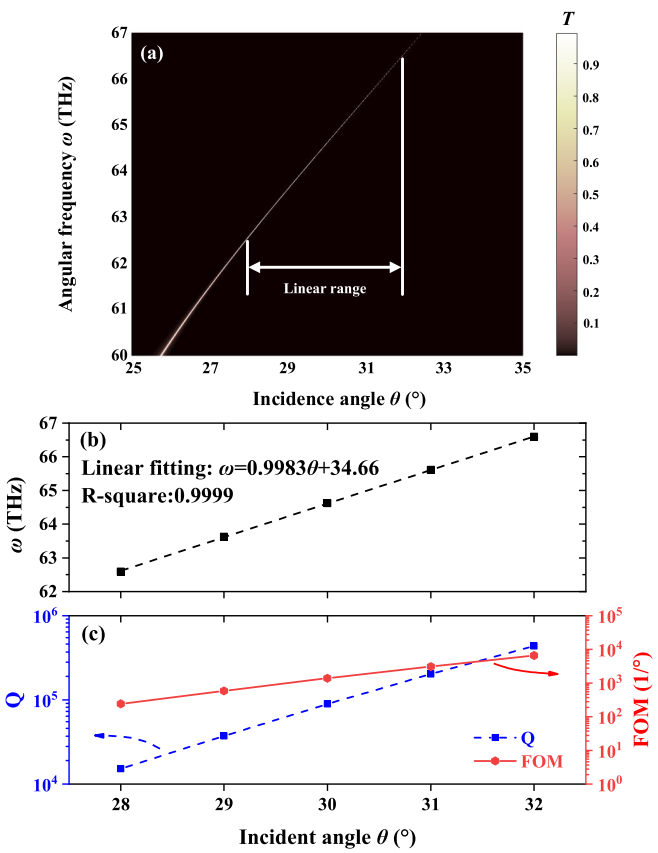

Fig. 7. (a) Transmission spectrum of the sensor at different incident angles θ. (b) Transmission spectrum after fitting of linear range. (c) Corresponding Q and FOM at different θ values.

by D, the magnitude of δ is [23]

$$\delta = \frac{\omega}{c} D \tag{14}$$

where $c = 3 \times 10^8$ m/s is the speed of light in a vacuum. Since the reflection of EM waves in the module II occurs at the boundary between the prism A and the $InSb_2$ layer, the optical path difference D between the incoming and reflected waves is mainly determined by the optical path Δ_m of the EM waves propagating in dielectric C, and $\Delta_m = n_m d_m$. In summary, the absorption frequency point is theoretically related to the product of the thickness d_m and the refractive index n_m of dielectric C, i.e., the optical path Δ_m, with a multiplicative relationship in a certain range. In addition, the evanescent wave generated by module I is a spike with a half-height width (FWHM) of only 0.0007 THz, and the frequency variation of the absorption spectrum should also be within this range.

First of all, when measuring the thickness, dielectric C is set as an air layer ($n_m = 1$), and the differences between the measured and actual values are explained in Section II. The absorption spectra with altering d_m are plotted in Fig. 8(a), two distinct linear areas can be observed in the range displayed in it, and the periodicity of Fig. 8(a) will be investigated in the sections that follow. Taking the interval of $d_m = 0.12d$–$0.42d$ as an example, the equation $\omega = -0.001844 d_m + 64.6247$ is fulfilled by the link between ω and d_m, and R-square is 0.9932, as depicted in Fig. 8(b). Based on the trend of the two curves in Fig. 8(c), it can be judged that Q and FOM located in the middle of the linear interval are slightly higher than the two sides, where Q of each point is between 115 000 and 145 000, and the FOM stays between $3d^{-1}$ and $4d^{-1}$, $d = 30\ \mu\text{m} = 3 \times 10^{-5}$ m. Since the interfering light wave is generated by module I, the absorption spectrum in the interferometric absorption mode also continues the property of high Q of evanescent waves and can be even higher compared with the transmittance case.

It is not difficult to understand that, except for the case $\delta = \pi$, the value of A_s in (13) can be made to be 0 whenever δ is equal to an odd multiple of π ($\delta = (2k+1)\pi, k = 0, 1, 2, \ldots$). In this way, the fact that δ grows linearly with d_m inevitably causes a periodic variation in the absorption spectrum. Fig. 9 demonstrates the variation of absorptance due to different d_m values for $\omega = 64.624$ THz. The distance between the corresponding d_m when the absorbance reaches a maximum is $0.5614\,d$, which can also be regarded as the length of a period. Based on these conclusions, it can be inferred that the range of the structure for thickness measurement is theoretically infinite, and all of the relational equations in the linear range can be calculated by fitting. However, this raises the question of how to accurately measure thicknesses that fall outside the linear range. The solution comes from refractive index sensing.

Fixing the thickness of the dielectric C layer to $0.6d$, it can be seen from (13) and (14) that the effects of the change in refractive index and thickness are equivalent to the combined amplitude, so that results for sensing the refractive

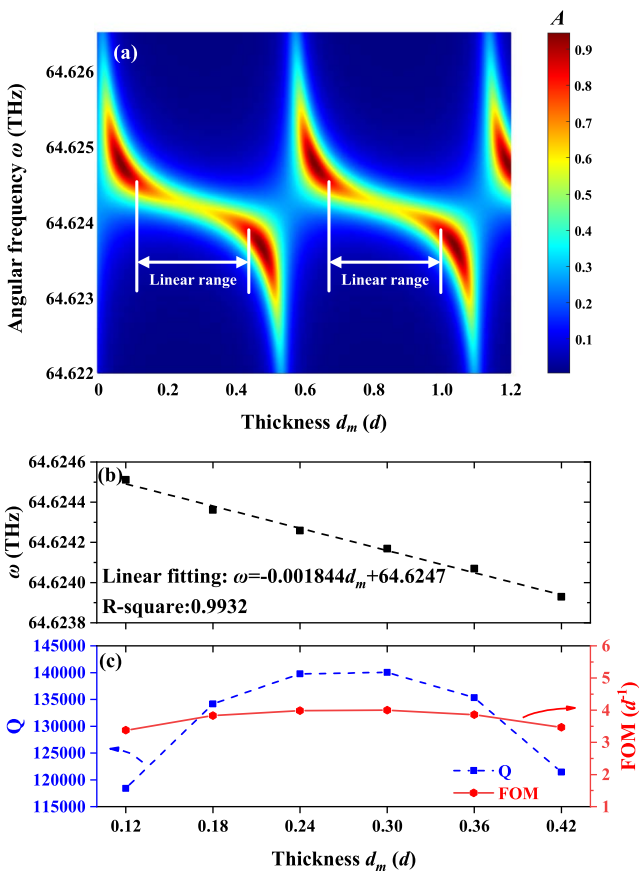

Fig. 8. (a) Absorption spectrum of the sensor at different thicknesses of the dielectric C layer d_m. (b) Absorption spectrum after fitting of linear range. (c) Corresponding Q and FOM at different d_m values.

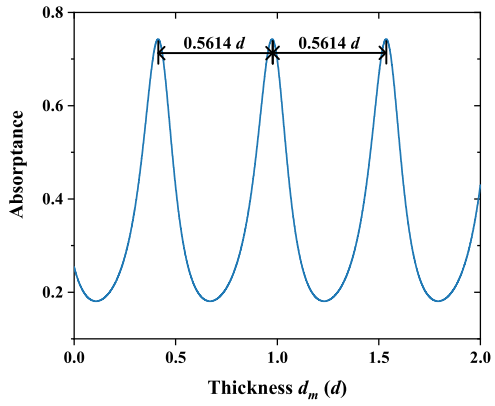

Fig. 9. Absorbance curves at different d_m values for $\omega = 64.624$ THz.

index can be obtained that are virtually identical to those for the thickness as Fig. 10(a)–(c). There are plural linear ranges in the absorption spectrum, the first of which is fit into the equation $\omega = -0.002438n_m + 64.6272$ with R-square $= 0.9916$. However, it is worth noting that in this case, the FOM is generally between 4 and 6 RIU^{-1}, which is not a relatively high value, although increasing the range of frequency variation can improve this situation, but also lead to a decrease in Q of other physical quantities. The design of the device in this regard requires certain trade-offs depending on the actual situation.

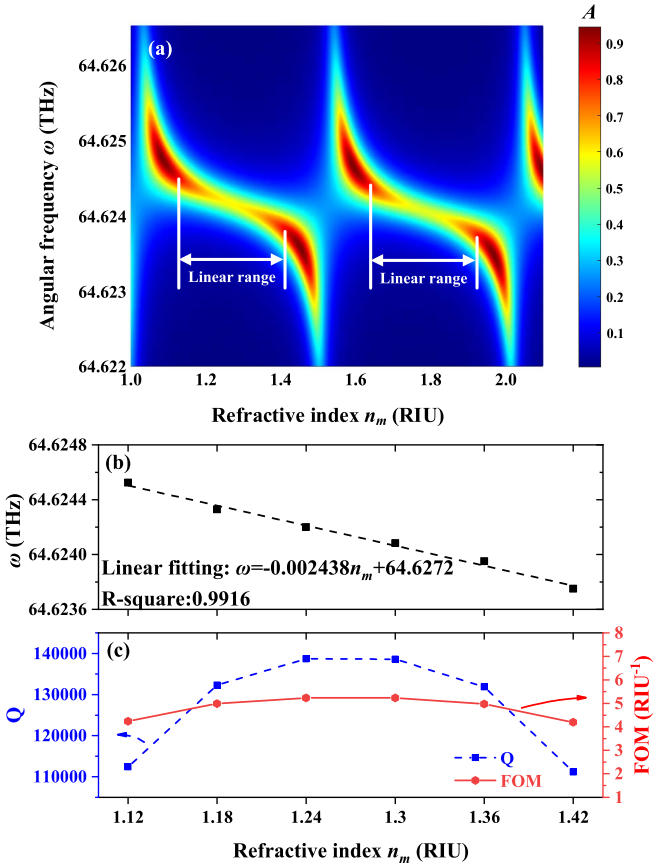

Fig. 10. (a) Absorption spectrum of the sensor at different refractive indexes of the dielectric C layer n_m. (b) Absorption spectrum after fitting of linear range. (c) Corresponding Q and FOM at different n_m values.

Now back to the previous question, since the distribution of the absorption spectrum ultimately depends on the optical path difference D, and it is shown that controlled by both the thickness and the refractive index of the dielectric C layer, the linear range issue is resolved. Using the sense of thickness, as an illustration, dielectric C defaults to air during the calculation; at this moment, the increase or decrease in n_m will necessarily cause the linear range to shift to the left or right simultaneously. If the approximate range of the value to be measured is known, the linear range can be adjusted by introducing other refractive index dielectrics to derive the accurate value. The same method can also be used for refractive index measurements.

IV. Conclusion

In summary, this work proposes a dual-mode multiphysical quantity sensor based on the InSb PCs. The use of the evanescent wave and interference principles allows for high-Q sensing of five physical quantities: magnetic field strength, thermodynamic temperature, incident angle, thickness, and refractive index. The whole structure can be subdivided into two modules according to the difference in functions, and the operating mode can be adjusted to switch between transmittance and interference absorption by changing the applied magnetic field. Among them, the transmittance mode is used for sensing the first three physical quantities, while the thickness and refractive index of dielectric C rely on the

interference absorption mode. It is worth mentioning that the measurement range of thickness and refractive index sensing can reach infinity in theory, and the linear range is tunable. In the trend of sensor design toward multimodal, multifunctional, and multiphysical quantities, this work provides positive insights.

REFERENCES

[1] H. Chu et al., "Band engineering method to create Dirac cones of accidental degeneracy in general photonic crystals without symmetry," *Opt. Exp.*, vol. 29, pp. 18070–18080, Jun. 2021.

[2] G. Lu et al., "Omnidirectional photonic bandgap in one-dimensional photonic crystals containing hyperbolic metamaterials," *Opt. Exp.*, vol. 29, pp. 31915–31923, Sep. 2021.

[3] J. Jin, J. Lu, and B. Zhen, "Resonance-forbidden second-harmonic generation in nonlinear photonic crystals," *Nanophotonics*, vol. 10, no. 17, pp. 4232–4239, 2021.

[4] A. H. Aly, S. E. S. A. Ghany, B. M. Kamal, and D. Vigneswaran, "Theoretical studies of hybrid multifunctional $YaBa_2Cu_3O_7$ photonic crystals within visible and infra-red regions," *Ceram. Int.*, vol. 46, no. 1, pp. 1012–1016, 2020.

[5] A. H. Aly, S. K. Awasthi, M. A. Mohaseb, Z. S. Matar, and A. F. Amin, "MATLAB simulation-based theoretical study for detection of a wide range of pathogens using 1D defective photonic structure," *Crystals*, vol. 12, no. 2, p. 220, Feb. 2022.

[6] S. Zlatanovic et al., "Photonic crystal microcavity sensor for ultracompact monitoring of reaction kinetics and protein concentration," *Sens. Actuators B, Chem.*, vol. 141, no. 1, pp. 13–19, 2009.

[7] B. Wan, H. Zhang, and P. Wang, "Nonreciprocal absorber with a narrow band of angular polarization sensitive regions based on a quasi-periodic structure," *Opt. Lett.*, vol. 46, pp. 1934–1937, Apr. 2021.

[8] S. R. Qutb, A. H. Aly, and W. Sabra, "Salinity and temperature detection for seawater based on a 1D-defective photonic crystal material," *Int. J. Modern Phys. B*, vol. 35, no. 1, Jan. 2021, Art. no. 2150012.

[9] S. E.-S. Abd El-Ghany, W. M. Noum, Z. S. Matar, Z. A. Zaky, and A. H. Aly, "Optimized bio-photonic sensor using 1D-photonic crystals as a blood hemoglobin sensor," *Phys. Scripta*, vol. 96, no. 3, Dec. 2020, Art. no. 035501.

[10] Z. Chen et al., "High power and narrow vertical divergence laser diodes with photonic crystal structure," *IEEE Photon. Technol. Lett.*, vol. 33, no. 8, pp. 399–402, Apr. 15, 2021.

[11] Y. Zhang and X. Bu, "Narrow linewidth erbium-doped fiber laser incorporating with photonic crystal fiber based Fabry–Pérot interferometer for temperature sensing applications," *Optik*, vol. 219, Oct. 2020, Art. no. 165005.

[12] L. Zhang et al., "Photonic crystal based on Mott phase change material as all-optical bandgap switch and composite logic gate," *Opt. Mater.*, vol. 113, Mar. 2021, Art. no. 110855.

[13] S. Edappadikkunnummal, R. C. Vasudevan, S. Dinesh, S. Thomas, N. R. Desai, and S. Kaniyarakkal, "Detection of hemoglobin concentration based on defective one-dimensional photonic crystals," *Photonics*, vol. 9, no. 9, p. 660, Sep. 2022.

[14] D. Ge, H. Chen, Z. Hu, J. Shi, and L. Zhang, "A new one-dimensional photonic crystal magnetic sensor based on magnetic fluid film with excellent sensing ability and figure of merit," *J. Magn. Magn. Mater.*, vol. 545, Mar. 2022, Art. no. 168753.

[15] S. Elshahat, Z. E. A. Mohamed, M. Almokhtar, and C. Lu, "High tunability and sensitivity of 1D topological photonic crystal heterostructure," *J. Opt.*, vol. 24, no. 3, Mar. 2022, Art. no. 035004.

[16] A. Sharma, S. Xie, R. Zeltner, and P. J. St Russell, "On-the-fly particle metrology in hollow-core photonic crystal fibre," *Opt. Exp.*, vol. 27, pp. 34496–34504, Nov. 2019.

[17] C.-Z. Li, S.-B. Liu, X.-K. Kong, H.-F. Zhang, B.-R. Bian, and X.-Y. Zhang, "A novel comb-like plasma photonic crystal filter in the presence of evanescent wave," *IEEE Trans. Plasma Sci.*, vol. 39, no. 10, pp. 1969–1973, Oct. 2011.

[18] Y.-T. Fang and Z.-C. Liang, "Unusual transmission through usual one-dimensional photonic crystal in the presence of evanescent wave," *Opt. Commun.*, vol. 283, no. 10, pp. 2102–2108, May 2010.

[19] T. Li, C. Yin, and F. Wu, "Strong optical non-reciprocity in one-dimensional photonic crystal containing a weyl semimetal-based defect," *Opt. Mater.*, vol. 121, Nov. 2021, Art. no. 111583.

[20] S. Chen, F. Fan, X. Wang, P. Wu, H. Zhang, and S. Chang, "Terahertz isolator based on nonreciprocal magneto-metasurface," *Opt. Exp.*, vol. 23, pp. 1015–1024, Jan. 2015.

[21] L. Qi, Z. Yang, F. Lan, X. Gao, and Z. Shi, "Properties of obliquely incident electromagnetic wave in one-dimensional magnetized plasma photonic crystals," *Phys. Plasmas*, vol. 17, no. 4, Apr. 2010, Art. no. 042501.

[22] Y. Zhao, M. Sheng, Y. Zheng, M. Xu, H. Zhao, and L. Chen, "Lateral shift effect on the spatial interference of light wave propagating in the single-layered dielectric film," *Opt. Exp.*, vol. 18, pp. 10524–10537, May 2010.

[23] G. Giusfredi, "Interference," in *Physical Optics*. Cham, Switzerland: Springer, 2019.

[24] H. Dai and Q. Liu, "Transfer matrix method and dispersive formula of light in thin films," *Proc. SPIE*, vol. 7282, May 2009, Art. no. 72820M.

Jia-Tao Zhang was born in Jiangsu, China, in 2001. He is currently pursuing the master's degree with the Nanjing University of Posts and Telecommunications, Nanjing, China.

His research interests include cylindrical photonic crystals.

Si-Si Rao was born in Hubei, China, in 2001. She is currently pursuing the master's degree with the Nanjing University of Posts and Telecommunications. Nanjing, China, on investigating nonlinear photonic crystals and evanescent wave.

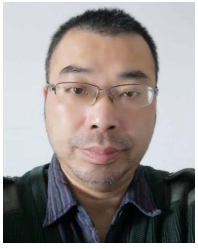

Hai-Feng Zhang was born in Jiangxi, China, in 1978. He received the M.Sc. degree in electronics science and technology from Nanchang University, Nanchang, China, in 2008, and the Ph.D. degree from the College of Electronic and Information Engineering, Nanjing University of Aeronautics and Astronautics, Nanjing, China, in 2014.

He is a Professor with the College of Electronic and Optical Engineering and the College of Flexible Electronics, Nanjing University of Posts and Telecommunications, Nanjing. His main research interests include the computational electromagnetics, plasma photonic crystals, plasma stealthy, and the electromagnetic properties of metamaterials.